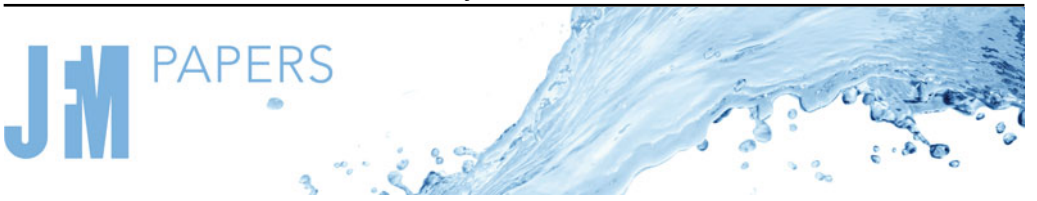
J. Fluid Mech. (2026), *vol.* 1046, A41, doi:10.1017/jfm.2026.12225



Competition between diffusive damping and instability growth in a rarefied Rayleigh–Taylor system

Zeqi Shi[1,†], **Hao Jiang**[1,†], **Yuan Ma**[1], **Kai Leong Chong**[1,2] and **Quan Zhou**[1]

[1]Shanghai Institute of Applied Mathematics and Mechanics, School of Mechanics and Engineering Science, and Shanghai Key Laboratory of Mechanics in Energy Engineering, Shanghai University, Shanghai 200072, PR China

[2]Shanghai Institute of Aircraft Mechanics and Control, Zhangwu Road, Shanghai, 200092, PR China

Corresponding author: Kai Leong Chong, klchong@shu.edu.cn

(Received 31 December 2025 UTC; revised 26 May 2026 UTC; accepted 21 September 2026 UTC)

The mechanisms underlying the generation and evolution of Rayleigh–Taylor instability (RTI) in rarefied gases are an important issue, particularly in many emerging problems where rarefaction effects become significant. Using a graphics processing unit parallelised direct simulation Monte Carlo approach, we simulate RTI across a wide range of Knudsen numbers (Kn), and find that instability growth is progressively inhibited as Kn increases, with complete suppression above a critical value $Kn \approx 0.011$. Molecular-scale analysis reveals that rarefaction enhances super-diffusive transport of the molecules, extending the ballistic regime, and favouring the interfacial mixing. This microscale behaviour macroscopically manifests as a rapid decay of the density gradient and the effective Atwood number. To determine whether instability emerges in rarefied conditions, we introduce a stability criterion based on the competition between a diffusive time scale (τ_D) and an instability time scale (τ_I). The transition to instability occurs only when $\tau_I < \tau_D$, a condition that fails for $Kn \gtrsim 0.011$. The effect of domain height is interpreted through its influence on the Froude number (Fr). Small domains (large Fr) hinder the transition from linear to nonlinear growth, while for larger domains, instability suppression is mainly determined by the threshold Knudsen number. The critical threshold $Kn \approx 0.011$ remains consistent for sufficiently small Fr. These findings provide a multiscale perspective on flow instability in rarefied gases, and establish a time scale competition framework that quantitatively explains how rarefaction governs the onset of RTI.

Key words: instability, rarefied gas flow, gas dynamics

[†]These authors contributed equally to this work.

© The Author(s), 2026. Published by Cambridge University Press.

https://doi.org/10.1017/jfm.2026.12225 Published online by Cambridge University Press

1. Introduction

Rayleigh–Taylor instability (RTI) evolves at the interface of two fluids with different densities when a heavier fluid is above a lighter one under an external acceleration normal to the interface, typically gravity. Similar to Rayleigh–Bénard convection – where buoyancy drives motion in a fluid layer heated from below (Ahlers *et al.* 2009; Lohse & Xia 2010; Chillà & Schumacher 2012; Shishkina 2021; Lohse & Shishkina 2023, 2024; Xia *et al.* 2023; Xia *et al.* 2025) – RTI is a fundamental buoyancy-driven instability. The occurrence of RTI can be seen in natural systems and engineering applications (Zhou 2017*a*,*b*), including the geophysical formation of volcanic islands (McGuire 1996; Zhang *et al.* 2018), atmospheric circulation (Wunsch & Ferrari 2004; Boffetta & Mazzino 2017), and the hydrodynamic behaviour of liquid films (Livescu *et al.* 2011).

The traditional studies on RTI typically rely on the continuum assumption. However, rarefaction effects become significant in many emerging problems, where the Knudsen number ($Kn = l/L$) quantifies the degree of rarefaction based on the molecular mean free path l and a characteristic length scale L. This is particularly relevant in astrophysics (Janka 2012; Isobe *et al.* 2015; Ma *et al.* 2015), nuclear collisions (Bouras *et al.* 2012), inertial confinement fusion (Betti & Hurricane 2016; Larroche *et al.* 2016), and the expansion of tin plasma under a low pressure environment in extreme-ultraviolet light lithography (Theofanous *et al.* 2004; Bakshi 2006; Rao & Basu 2026; Chong *et al.* 2026). Overall, the continuum descriptions become invalid when Kn is sufficiently large, which can be achieved in high vacuum or microscale environments.

As early as the 1880s, Rayleigh (1883) showed mathematically that when a heavier fluid overlies a lighter one, the interface between them becomes unstable. Subsequent studies demonstrated that the evolution of this interfacial instability depends on gravitational acceleration, density contrast and initial perturbations. Building on Rayleigh's analysis, Taylor (1950) experimentally quantified how the instability growth rate varies with perturbation wavelength, acceleration and density contrast, thereby laying the foundation for modern hydrodynamic instability theory. The evolution of RTI is commonly divided into three stages based on growth behaviour: the linear stage, the nonlinear growth stage, and the self-similar regime (Ristorcelli & Clark 2004; Zhou & Jiang 2016; Boffetta & Mazzino 2017; Zhou *et al.* 2021). The relationship between the mixing layer width and time across these stages has been confirmed through both theoretical and experimental results (Layzer 1955; Zhou *et al.* 2016). Wei & Livescu (2012) employed direct numerical simulations (DNS) to simulate two-dimensional RTI with a single-mode, fixed-wavelength perturbation at the initial interface, providing a detailed analysis of how the Reynolds number influences RTI growth rates across different stages.

Moreover, it was found that at low Reynolds numbers, both dynamic viscosity and diffusion exert a strong inhibitory effect on the growth of instabilities. Accordingly, Duff *et al.* (1962) derived a modified growth rate expression for gas-phase RTI that accounts for viscous and diffusive effects. To investigate the microscopic mechanisms underlying interfacial instability formation, Kadau *et al.* (2004, 2007, 2008, 2010) used molecular dynamics and direct simulation Monte Carlo (DSMC) to simulate RTI with an initially flat interface in continuous flow. Their results were consistent with theoretical predictions and experimental observations, while also showing that molecular scale fluctuations play an increasingly important role as system size decreases. Gallis *et al.* (2016) further applied DSMC to simulate RTI flows, and examined the evolution of flat and single-mode initial interfaces under varying Atwood numbers and gravitational accelerations at low Kn values. Their study demonstrated that across the linear, nonlinear and self-similar regimes, DSMC agree well with theoretical and experimental results, and that molecular level perturbations significantly influence the growth of interfacial perturbations.

https://doi.org/10.1017/jfm.2026.12225 Published online by Cambridge University Press

Although extensive research has been conducted on RTI, the vast majority of studies rely on the continuum assumption. Consequently, studies on RTI in rarefied environments remain limited, despite their emerging relevance in modern applications. Kashkovsky *et al.* (2019) employed the DSMC method to simulate an RTI system with an initially flat interface under low pressure conditions. At $Kn = 0.0036$, the instability growth characteristics were found to closely match continuum flow predictions, a conclusion also supported by Shershnev *et al.* (2023, 2024). Although their RTI study used a low-pressure gas, the Knudsen numbers were relatively small ($Kn < 0.01$). Consequently, these cases exhibit only relatively weak rarefaction effects. Sagert *et al.* (2014, 2015) used an extended DSMC formulation to simulate RTI with fixed wavelength initial perturbations under different Kn. Their results indicated that at large Kn, enhanced molecular diffusion suppresses secondary growth of the interfacial instability. However, these studies did not account for the thermally driven most unstable wavelength, which increases with Kn (Duff *et al.* 1962). When this most unstable wavelength exceeds the initially fixed perturbation wavelength, it dominates the RTI evolution, but this behaviour cannot be captured within a fixed computational domain. Only a limited number of studies have examined rarefaction effects in RTI. In particular, the coupling between molecular scale fluctuations in transitional flows and macroscopic hydrodynamic instabilities is poorly understood, making it challenging to assess how rarefaction alters RTI evolution.

According to the classical classification of rarefied gas flows (Bird 1994; Gad-el-Hak 1999), the continuum assumption is generally valid only for $Kn < 0.001$. In the slip flow regime ($Kn > 0.001$), DSMC results show better agreement with experimental measurements than the corresponding Navier–Stokes (NS) predictions (Stefanov *et al.* 2005; Gallis *et al.* 2006; Li *et al.* 2019). To systematically study the evolution of RTI in rarefied gases, we employ the DSMC method to simulate a two-dimensional Rayleigh–Taylor (RT) system with an initially flat interface over a range of Knudsen numbers. Moreover, considering that DSMC require a huge number of particles (in excess of hundreds of millions) to reduce statistical noise, a graphics processing unit (GPU) parallelised DSMC method is adopted to enhance computational efficiency (Gladkov *et al.* 2012; Norman *et al.* 2013). The objective of this study is to examine how the degree of rarefaction influences the evolution of RTI and the threshold mechanisms for instability onset in rarefied gases.

The remainder of this paper is organised as follows. Section 2 presents the governing equations and numerical set-up. Section 3 investigates the evolution of RTI under varying Knudsen numbers, including molecular transport behaviour, macroscopic flow characteristics, and the competition between diffusive damping and instability growth. The influence of the computational height is further examined by varying the Froude number Fr. Section 4 summarises the main conclusions and outlook.

2. Numerical methods and problem set-up

2.1. *The DSMC*

Rarefied gas flows have been investigated using a variety of numerical approaches in recent years (Xu & Huang 2010; Gorji *et al.* 2011; Fei *et al.* 2020; Su *et al.* 2020). Among these methods, the DSMC method developed by Bird (1963, 1994) is particularly well suited for problems involving strong non-equilibrium effects, as it directly resolves molecular transport processes such as viscosity, thermal conductivity and mass diffusion. Owing to these characteristics, DSMC has been extensively validated against theoretical predictions over a wide range of Knudsen numbers, from near-continuum to highly rarefied regimes (Garcia 1986; Gallis *et al.* 2016; McMullen *et al.* 2022; Ma *et al.* 2024). In the context of RTI at finite Knudsen numbers, where compressibility and non-equilibrium molecular

https://doi.org/10.1017/jfm.2026.12225 Published online by Cambridge University Press

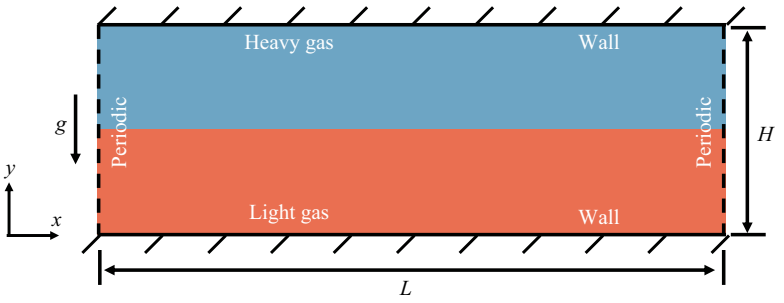


Figure 1. Sketch of the set-up of the RTI system.

effects may play a significant role, DSMC provides a physically consistent framework for capturing the underlying gas dynamics.

Based on the above considerations, DSMC is employed in this work to simulate a two-dimensional RTI with an initially flat interface at various Knudsen numbers. A schematic of the computational set-up and the corresponding initial and boundary conditions is shown in figure 1. The heavy fluid initially occupies the upper half of the computational domain, while the light fluid occupies the lower half. Gravity acts in the negative y-direction and normal to the interface. The boundaries at $y = 0$ and $y = H$ are treated as solid walls, whereas periodic boundary conditions are prescribed at $x = 0$ and $x = L$.

In DSMC, particle transport and collisions are treated separately, which requires the time step to be smaller than the mean collision time, and the cell size to be smaller than the molecular mean free path l (Bird 1994; Goshayeshi *et al.* 2020; Ma *et al.* 2024). The initial particle positions and velocity distributions are prescribed according to the macroscopic properties of the gas. To ensure both spatial uniformity and randomness at the particle level, equal numbers of particles are placed in each computational cell, and their positions are randomly assigned within the cell. The particle velocities are sampled according to the Maxwell–Boltzmann distribution. The corresponding probability density function $f(u)$ for the particle speed is given by (Cercignani 1988)

$$f(u) = 4\pi \left(\frac{m_i}{2\pi k_B T} \right)^{3/2} \exp^{-\frac{m_i u^2}{2k_B T}} u^2, \tag{2.1}$$

where m_i is the mass of a molecule of species i, k_B is the Boltzmann constant, T is the absolute temperature, and u denotes the magnitude of the molecular speed.

Since particle transport and collisions are decoupled in DSMC, particle motion within a time step Δt is treated as ballistic motion. The Maxwell diffuse reflection model can be used to describe particle–wall interactions (Bird 1994; Goshayeshi *et al.* 2020; McMullen *et al.* 2023). After particle transport and boundary processing, particles are reassigned to their corresponding collision cells. To model particle–particle collisions, each collision cell is further subdivided into several subcells. Within each subcell, particle pairs are selected probabilistically according to the adopted collision model. In this study, the variable soft-sphere (VSS) model is employed to calculate the particle collision frequency (Koura & Matsumoto 1992; Stevens & Hrenya 2005; Gallis *et al.* 2021; Ma *et al.* 2024). For a multi-component gas mixture consisting of s species, the total number of collisions per unit volume and per unit time is given by

$$N_c = \frac{1}{2} \sum_{i=1}^{s} (n_i z_i), \tag{2.2}$$

https://doi.org/10.1017/jfm.2026.12225 Published online by Cambridge University Press

where n_i denotes the number density of molecules of component i, and z_i denotes the collision frequency of molecules of component i. The collision frequency is expressed as

$$z_i = \sum_{j=1}^{s} (n_j \overline{\pi d_{ij}^2 u_{r_{ij}}}), \tag{2.3}$$

where d_{ij} is the effective collision diameter between molecular species i and j, and $u_{r_{ij}}$ is the relative speed between pairs of collision particles. The overline denotes an ensemble average over the distribution of molecular velocities.

To ensure that molecular diffusion and viscosity are correctly represented in the DSMC framework, the VSS model combined with the first-order Chapman–Enskog expansion is adopted to relate collision parameters to macroscopic transport coefficients (Koura & Matsumoto 1992; Bird 1994). The dynamic viscosity μ is given by

$$\mu = \frac{5(\alpha+1)(\alpha+2)(\pi m k_B)^{1/2}(4k_B/m)^{\xi} T^{1/2+\xi}}{16\alpha\Gamma(4-\xi)\sigma_{T,ref} u_{r,ref}^{2\xi}}, \tag{2.4}$$

and the binary diffusion coefficient D_{12} is expressed as

$$D_{12} = \frac{3\,(\alpha_{12}+1)\,\pi^{1/2}\,(2k_B T/m_r)^{\omega_{12}}}{16\Gamma\,(7/2-\omega_{12})\,n\,\left(\sigma_{T,ref}\right)_{12}\,u_{r,ref}^{2(\omega_{12}-1/2)}}, \tag{2.5}$$

where α and ω are the VSS scattering parameters, subscripts 1 and 2 denote the two molecular species, and $\omega = 1/2 + \xi$. Here, the reduced mass is $m_r = m_1 m_2/(m_1+m_2)$, the reference collision cross-section is $\sigma_{T,ref} = \pi d^2$, and $u_{r,ref}$ is the reference relative velocity. Additional parameter definitions and the properties of the Γ function are provided in Bird (1994).

A known limitation of the DSMC method is the presence of statistical noise arising from the finite number of simulation particles. When each particle represents a real molecule, the statistical noise inherently accounts for the influence of molecular thermal fluctuations on the macroscopic flow field (Gallis *et al.* 2016; Liao & Qin 2022, 2025). The statistical uncertainty decreases with increasing sample size, and can be reduced through ensemble averaging. In this study, all particles residing in a computational cell over a prescribed sampling interval are collected for ensemble averaging, from which macroscopic quantities such as density, velocity, pressure and temperature are evaluated. Since the RT system considered here involves two molecular species, their contributions are treated separately in both collision calculations and statistical evaluations of macroscopic variables.

2.2. *Verification of the DSMC code*

The evolution of the RTI is governed by gravitational acceleration and fluid properties. According to linear stability theory (Taylor 1950; Gallis *et al.* 2016; Boffetta & Mazzino 2017), the perturbation growth rate is

$$\gamma_0 \approx \sqrt{A_t g k}, \quad k = 2\pi/\lambda, \tag{2.6}$$

where g is the gravitational acceleration, k is the wavenumber, and λ is the perturbation wavelength. The Atwood number $A_t = (\rho_h - \rho_l)/(\rho_h + \rho_l)$ quantifies the density contrast between the heavy (ρ_h) and light (ρ_l) fluids. The corresponding characteristic time scale is $\tau = 1/\gamma_0$ (Youngs 1984). Equation (2.6) indicates that shorter perturbation wavelengths lead to larger growth rates. However, viscosity and diffusion inhibit the growth of short-wavelength perturbations. For an initially flat interface, molecular thermal fluctuations are amplified and trigger the instability. These perturbations encompass a wide range of

https://doi.org/10.1017/jfm.2026.12225 Published online by Cambridge University Press

wavelengths, with the most unstable mode exhibiting the fastest growth rate. The most unstable wavelength λ_m of the RT system is given by (Sharp 1984; Youngs 1984)

$$\lambda_m \approx 4\pi \left(\frac{\bar{\nu}^2}{A_t g} \right)^{1/3}, \tag{2.7}$$

where $\bar{\nu} = (\mu_h + \mu_l)/(\rho_h + \rho_l)$ is the mean kinematic viscosity, and μ_h and μ_l denote the dynamic viscosities of the heavy and light fluids, respectively. During the early linear stage of the instability, the perturbation amplitude a evolves according to linear stability theory given by (Taylor 1950; Gallis *et al.* 2016)

$$a = a_0 \cosh(t\sqrt{A_t g k}), \tag{2.8}$$

where a_0 is the initial perturbation amplitude.

In a gaseous RT system, the kinematic viscosity, diffusion coefficient and density contrast strongly influence the growth of initial interfacial perturbations. Duff *et al.* (1962) corrected the growth rate by accounting for the influence of diffusion on interface instability. The growth rate γ_0 can be expressed as

$$\gamma_0 = \sqrt{A_t g k + \bar{\nu}^2 k^4} - (\bar{\nu} + D_{12})k^2, \tag{2.9}$$

where γ_0 has maximum value at a specific wavenumber k. This wavenumber corresponds to the most unstable wavelength λ_m for an initially flat interface. Accordingly, (2.9) is used to determine λ_m in this study.

In the nonlinear stage ($ka \sim 1$), following Layzer (1955), Goncharov (2002) and Mikaelian (2014), the bubble amplitude a_b and spike amplitude a_s are expressed as

$$a_b(A_t) = a_0 + \left(\frac{3 + A_t}{3(1 + A_t)k} \right) \ln \left[\cosh \left(t \frac{\sqrt{6gkA_t(1 + A_t)}}{3 + A_t} \right) \right], \tag{2.10}$$

$$a_s(A_t) = a_b(A_t) \left(1 + \left[0.4 + 0.6A_t^{10} \right] \left[\left(\frac{a_s(1)}{a_b(A_t)} \right)^{A_t} - 1 \right] \right). \tag{2.11}$$

In the self-similarity stage, experimental data indicate that the growth rates of bubbles and spikes can be described by a simple model (Cook *et al.* 2004; Ristorcelli & Clark 2004; Boffetta & Mazzino 2017)

$$a_{b,s} = \alpha_{b,s} A_t g t^2, \tag{2.12}$$

where α_b is approximately 0.005, and α_s depends on A_t. The total interface amplitude is given by $a = a_b + a_s$.

To validate the code, a GPU parallel DSMC method was employed to simulate the RT system with initially fixed perturbation wavelengths λ. The relevant gas and RT system parameters are summarised in tables 1 and 2, respectively (Gallis *et al.* 2016). The evolution of the interface height over time is shown in figure 2. The amplitude of interface perturbations as a function of time agrees well with both linear and nonlinear theories, and is consistent with the DSMC results (Gallis *et al.* 2016). Further comparison with NS results at different Knudsen numbers shows that DSMC and NS predictions are in good agreement under continuum flow conditions, as shown in figure 2(*c*). However, in the slip flow regime ($0.001 < Kn < 0.013$), the NS results deviate significantly from the DSMC predictions, as shown in figure 2(*d*). This discrepancy arises because the NS equations cannot accurately capture the non-equilibrium molecular transport processes occurring in the slip flow regime, thereby demonstrating the advantage of DSMC in this

https://doi.org/10.1017/jfm.2026.12225 Published online by Cambridge University Press

Gas	m (kg)	d (m)	ρ (kg m^{-3})	μ (Pa s)	ν (m^2 s^{-1})	ω	α
He	6.65×10^{-27}	2.30×10^{-10}	0.179	1.865×10^{-5}	10.4×10^{-5}	1.26	0.66
Ar	66.35×10^{-27}	4.11×10^{-10}	1.781	2.117×10^{-5}	1.19×10^{-5}	1.4	0.81

Table 1. Properties of pure gas at $P = 101\,325$ Pa and $T = 273.15$ K. Here, ω and α are the parameters of the VSS molecular collision model (Bird 1994).

Gases	A_t	g (m s^{-2})	λ (mm)	a_0 (μm)	P_{ref} (Pa)	T (K)
Ar/He	0.82	1.0×10^8	1.00	10.0	101 325	273.15

Table 2. Validation of RTI simulation at 1 mm $\times$ 4 mm domain. Here, P_{ref} is the initial interface reference pressure, and λ is the initial interface perturbation wavelength.

range. To further verify mesh independence, the RT system with an initially flat interface was simulated using meshes of different sizes. The relevant RT system parameters are summarised in table 3 (case 3). The results show that smaller grid sizes do not affect the characteristics of the interface evolution, as shown in figure 2(*b*). Therefore, this study adopts the standard DSMC requirements for mesh size and time step. The cell size satisfies $\Delta x < l/2$, and the simulation time step satisfies $\Delta t < 0.2\Delta x / V_{th}$ (Bird 1994; Gallis *et al.* 2016; Goshayeshi *et al.* 2020), where the molecular mean free path is given by $l = 1/\sqrt{2}\,\pi \bar{d}^2 n_{h,l}$ and $\bar{d} = 0.5(d_h + d_l)$.

2.3. *Problem configuration*

In this study, the kinematic viscosity and diffusion coefficient increase significantly as the gas becomes more rarefied. According to (2.9), the most unstable wavelength λ_m also increases. We first examined the sensitivity to the domain height ratio H/λ_m. According to Wei & Livescu (2012), linear stability theory is valid only when the interface height satisfies $a/\lambda_m \leqslant 0.4$ in the continuum regime. To investigate flow evolution beyond this linear regime, we fixed $H/\lambda_m = 0.5$ and simulated RTI for various Kn. The specific parameters for these simulations are summarised in cases 1–6 of table 3. To further examine the influence of the domain height, Betti *et al.* (1998) introduced the Froude number Fr as a control parameter for perturbation growth, defined as $Fr = V_{th}^2/(gH)$. Similarly, Zhou *et al.* (2016) used the Rayleigh number to characterise the relationship between domain size and instability. Following this approach, simulations were performed for different Fr and Kn, as summarised in cases 7–48 of table 3, where $V_{th} = \sqrt{2k_B T_{ref}/m}$ is the molecular thermal velocity, and $L = 1.5\lambda_m$. In the RT system, the heavy and light fluids are argon (Ar) and helium (He), respectively, and their properties at standard conditions are listed in table 1. The reference interface temperature is $T_{ref} = 273.15$ K. This significantly enhanced gravitational acceleration is applied to the system in order to accelerate the growth of RTI within the confined computational domain (Gallis *et al.* 2016; Goshayeshi *et al.* 2020). The initially flat interface is located at $y = H/2$. Then the pressure distribution is prescribed as

$$P_{h,l}(y) = P_{ref} + \rho_{h,l} g(0.5H - y). \tag{2.13}$$

Using the ideal gas equation of state, the temperature distribution along y is given by

$$k_B\, T_{h,l}(y) = P_{h,l}(y)/n_{h,l}, \tag{2.14}$$

https://doi.org/10.1017/jfm.2026.12225 Published online by Cambridge University Press

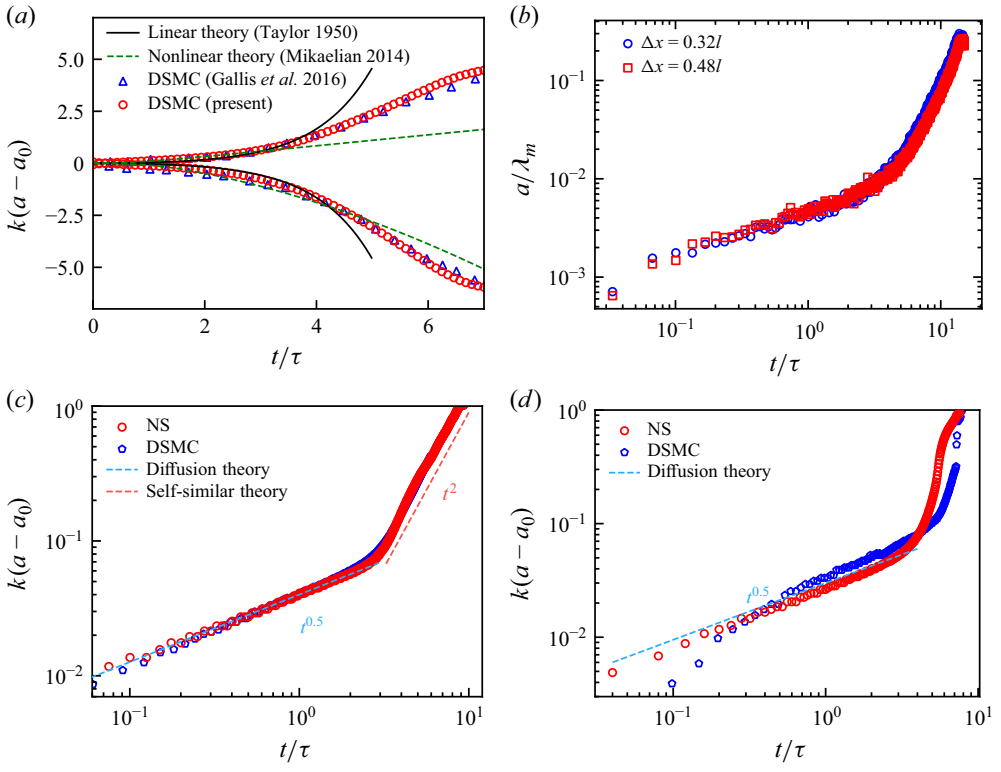


Figure 2. Verification of the DSMC. (*a*) The normalised perturbation amplitude $k(a - a_0)$ as a function of time t/τ. (*b*) Evolution of the interface height in an RT system with an initially flat interface under different grid resolutions for $Kn = 0.005$. (*c*) Comparison of DSMC and NS predictions for the interface evolution height at $Kn = 0.001$. (*d*) Comparison of DSMC and NS predictions for the interface evolution height at $Kn = 0.009$.

where $n_h = n_l$ at the reference state. The number densities are computed from the ideal gas relation $n_{h,l} = P_{ref}/(k_B T_{ref})$. Collision sampling at each time step is based on the 'no time counter' scheme (Bird 1989; Goshayeshi *et al.* 2020; Ma *et al.* 2024). To reduce statistical uncertainty, macroscopic variables are obtained by averaging 20 time step samples, and performing eight independent ensemble implementations (Goshayeshi *et al.* 2020; Ma *et al.* 2024). The simulation time exceeds the characteristic time at which interface growth ceases. A quasi-two-dimensional computational domain with thickness 100 nm is used to model the RT system, with each computational particle representing 1000 real gas molecules.

3. Results and discussion

In this section, we first investigate the influence of the Knudsen number on the RTI evolution under a fixed geometric condition $H/\lambda_m = 0.5$ (§§ 3.1–3.4). Based on these results, we further extend the analysis to examine the combined effects of the Knudsen number Kn and Fr on the instability dynamics (§ 3.5).

3.1. *Evolution of the interface at different Kn*

In RTI, the concentration field better captures the morphology of the evolving mixing layer between the heavy and light gases; we hereafter refer to this as the 'interface'. Figure 3 shows instantaneous snapshots of the normalised concentration field α_v for different Kn.

https://doi.org/10.1017/jfm.2026.12225 Published online by Cambridge University Press

Case	P_{ref} (Pa)	l (m)	g (m s^{-2})	λ_m (m)	τ (s)	H/λ_m	$Kn = l/H$	Fr
1	101 325	8.2×10^{-8}	1.4×10^{7}	1.4×10^{-4}	1.85×10^{-6}	0.5	1.0×10^{-3}	107
2	4000	2.1×10^{-6}	1.4×10^{7}	1.2×10^{-3}	5.42×10^{-6}	0.5	3.0×10^{-3}	12.4
3	1000	8.3×10^{-6}	1.4×10^{7}	3.0×10^{-3}	8.61×10^{-6}	0.5	5.0×10^{-3}	4.91
4	250	3.3×10^{-5}	1.4×10^{7}	7.6×10^{-3}	1.37×10^{-5}	0.5	8.0×10^{-3}	1.95
5	100	8.3×10^{-5}	1.4×10^{7}	1.4×10^{-2}	1.87×10^{-5}	0.5	1.1×10^{-2}	1.07
6	80	1.0×10^{-4}	1.4×10^{7}	1.6×10^{-2}	2.02×10^{-5}	0.5	1.3×10^{-2}	1.01
7	10 000	8.3×10^{-7}	1.4×10^{7}	6.4×10^{-4}	4.00×10^{-6}	0.4	3.1×10^{-3}	30.8
8	4000	2.1×10^{-6}	1.4×10^{7}	1.2×10^{-3}	5.42×10^{-6}	0.4	3.0×10^{-3}	16.7
9	1000	8.3×10^{-6}	1.4×10^{7}	3.0×10^{-3}	8.61×10^{-6}	0.4	6.7×10^{-3}	6.63
10	500	1.7×10^{-5}	1.4×10^{7}	4.7×10^{-3}	9.62×10^{-6}	0.4	8.6×10^{-3}	4.21
11	250	3.3×10^{-5}	1.4×10^{7}	7.6×10^{-3}	1.37×10^{-5}	0.4	1.1×10^{-2}	2.62
12	25 000	3.3×10^{-7}	1.4×10^{7}	3.5×10^{-4}	2.21×10^{-6}	0.22	4.4×10^{-3}	107
13	12 500	6.6×10^{-7}	1.4×10^{7}	5.6×10^{-4}	2.78×10^{-6}	0.14	8.7×10^{-3}	107
14	10 000	8.3×10^{-7}	1.4×10^{7}	6.4×10^{-4}	4.00×10^{-6}	0.12	1.1×10^{-2}	107
15	8400	9.8×10^{-7}	1.4×10^{7}	7.5×10^{-4}	4.23×10^{-6}	0.10	1.3×10^{-2}	107
16	10 000	8.3×10^{-7}	1.4×10^{7}	6.4×10^{-4}	4.00×10^{-6}	1.18	1.1×10^{-3}	10.7
17	2500	3.3×10^{-6}	1.4×10^{7}	1.6×10^{-3}	6.34×10^{-6}	0.47	4.4×10^{-3}	10.7
18	1250	6.6×10^{-6}	1.4×10^{7}	2.6×10^{-3}	7.99×10^{-6}	0.30	8.7×10^{-3}	10.7
19	1000	8.3×10^{-6}	1.4×10^{7}	3.0×10^{-3}	8.61×10^{-6}	0.25	1.1×10^{-2}	10.7
20	840	9.8×10^{-6}	1.4×10^{7}	3.4×10^{-3}	9.12×10^{-6}	0.23	1.3×10^{-2}	10.7
21	1000	8.3×10^{-6}	1.4×10^{7}	3.0×10^{-3}	8.61×10^{-6}	2.5	1.1×10^{-3}	1.07
22	250	3.3×10^{-5}	1.4×10^{7}	7.6×10^{-3}	1.38×10^{-5}	0.99	4.4×10^{-3}	1.07
23	125	6.6×10^{-5}	1.4×10^{7}	1.2×10^{-2}	1.74×10^{-5}	0.62	8.7×10^{-3}	1.07
24	109	7.6×10^{-5}	1.4×10^{7}	1.3×10^{-2}	1.81×10^{-5}	0.58	1.0×10^{-2}	1.07
25	100	8.3×10^{-5}	1.4×10^{7}	1.4×10^{-2}	1.87×10^{-5}	0.54	1.1×10^{-2}	1.07
26	91	9.1×10^{-5}	1.4×10^{7}	1.5×10^{-2}	1.94×10^{-5}	0.51	1.2×10^{-2}	1.07
27	84	9.8×10^{-5}	1.4×10^{7}	1.6×10^{-2}	1.98×10^{-5}	0.48	1.3×10^{-2}	1.07
28	712	1.2×10^{-5}	1.4×10^{7}	3.8×10^{-3}	9.69×10^{-6}	1.53	2.0×10^{-3}	1.4
29	285	2.9×10^{-5}	1.4×10^{7}	7.0×10^{-3}	1.31×10^{-5}	0.83	5.0×10^{-3}	1.4
30	178	4.6×10^{-5}	1.4×10^{7}	9.6×10^{-3}	1.54×10^{-5}	0.61	8.0×10^{-3}	1.4
31	142	5.8×10^{-5}	1.4×10^{7}	1.1×10^{-2}	1.66×10^{-5}	0.52	1.0×10^{-2}	1.4
32	130	6.4×10^{-5}	1.4×10^{7}	1.2×10^{-2}	1.71×10^{-5}	0.49	1.1×10^{-2}	1.4
33	119	6.9×10^{-5}	1.4×10^{7}	1.3×10^{-2}	1.76×10^{-5}	0.46	1.2×10^{-2}	1.4
34	110	7.5×10^{-5}	1.4×10^{7}	1.3×10^{-2}	1.81×10^{-5}	0.44	1.3×10^{-2}	1.4
35	1030	8.0×10^{-6}	1.4×10^{7}	3.0×10^{-3}	8.54×10^{-6}	1.33	2.0×10^{-3}	2.03
36	413	2.0×10^{-5}	1.4×10^{7}	5.4×10^{-3}	1.16×10^{-5}	0.74	5.0×10^{-3}	2.03
37	258	3.2×10^{-5}	1.4×10^{7}	7.4×10^{-3}	1.36×10^{-5}	0.54	8.0×10^{-3}	2.03
38	206	4.0×10^{-5}	1.4×10^{7}	8.6×10^{-3}	1.46×10^{-5}	0.47	1.0×10^{-2}	2.03
39	188	4.4×10^{-5}	1.4×10^{7}	9.2×10^{-3}	1.51×10^{-5}	0.44	1.1×10^{-2}	2.03
40	172	4.8×10^{-5}	1.4×10^{7}	9.6×10^{-3}	1.55×10^{-5}	0.41	1.2×10^{-2}	2.03
41	159	5.2×10^{-5}	1.4×10^{7}	1.0×10^{-2}	1.59×10^{-5}	0.39	1.3×10^{-2}	2.03
42	100	8.3×10^{-5}	2.8×10^{6}	2.4×10^{-2}	5.48×10^{-5}	1.57	2.2×10^{-3}	1.07
43	50	1.7×10^{-4}	2.8×10^{6}	3.8×10^{-2}	6.90×10^{-5}	0.99	4.4×10^{-3}	1.07
44	30	2.8×10^{-4}	2.8×10^{6}	5.4×10^{-2}	8.18×10^{-5}	0.70	7.3×10^{-3}	1.07
45	22	3.8×10^{-4}	2.8×10^{6}	6.3×10^{-2}	8.46×10^{-5}	0.61	9.9×10^{-3}	1.07
46	20	4.1×10^{-4}	2.8×10^{6}	7.1×10^{-2}	9.36×10^{-5}	0.54	1.1×10^{-2}	1.07
47	18	4.6×10^{-4}	2.8×10^{6}	7.6×10^{-2}	9.65×10^{-5}	0.50	1.2×10^{-2}	1.07
48	17	4.9×10^{-4}	2.8×10^{6}	7.9×10^{-2}	9.89×10^{-5}	0.48	1.3×10^{-2}	1.07

Table 3. Detailed parameters of the numerical simulations for different Kn and Fr. Here, l is the molecular mean free path, and τ is the characteristic time scale of the most unstable wavelength.

https://doi.org/10.1017/jfm.2026.12225 Published online by Cambridge University Press

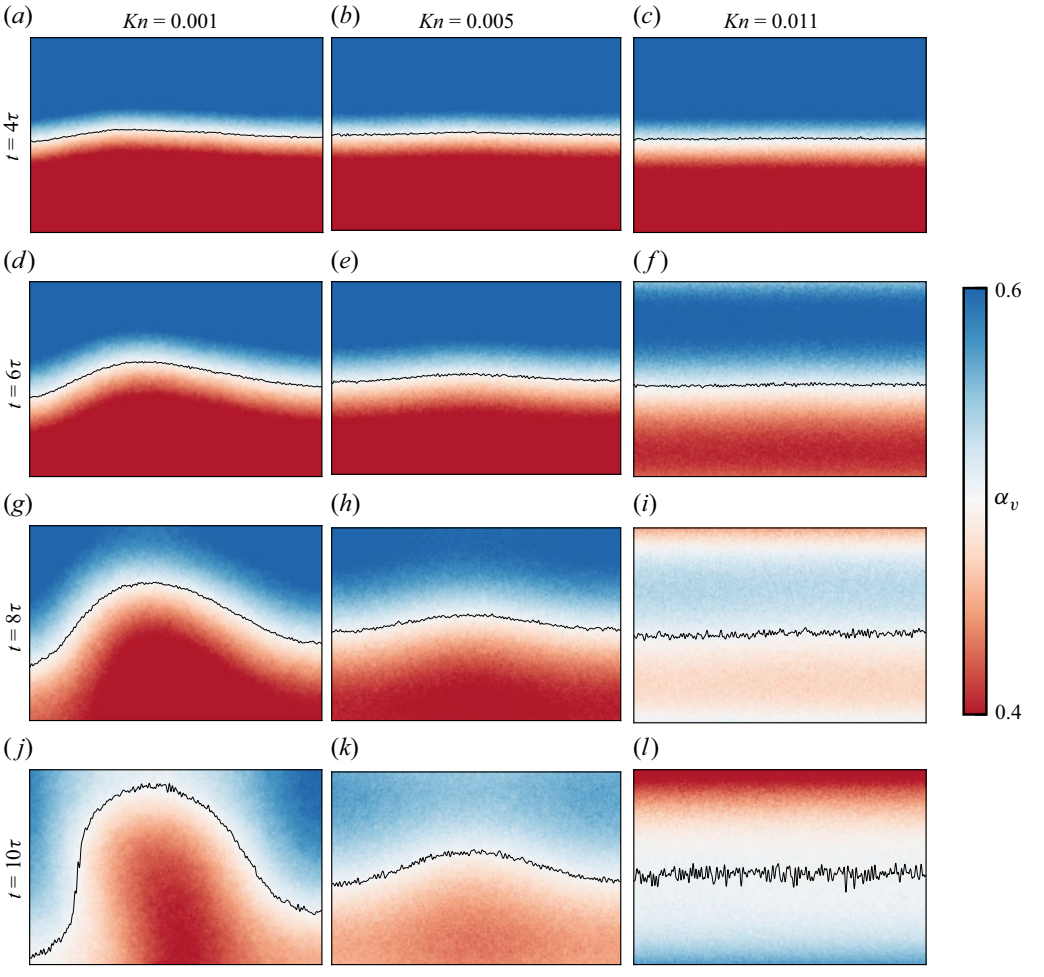


Figure 3. Typical snapshots of the normalised concentration field α_v at different Kn. The black solid line represents the interface position at $\alpha_v = 0.5$, and α_v represents the ratio of the number density n_h of the heavy fluid to the total number density n ($\alpha_v = n_h/(n_h + n_l)$). These correspond to $t = 4\tau$ in $(a{-}c)$, $t = 6\tau$ in $(d{-}f)$, $t = 8\tau$ in $(g{-}i)$, $t = 10\tau$ in $(j{-}l)$. Here, (a, d, g, j), (b, e, h, k) and (c, f, i, l) correspond to $Kn = 0.001$, 0.005 and 0.011, respectively.

Here, $\alpha_v = n_h/(n_h + n_l)$, where n_h and n_l denote the number densities of the heavy and light fluids, respectively. Each snapshot displays a subregion of the computational domain with a 3 : 2 aspect ratio. As shown in figures 3(a,d,g,j), when $Kn = 0.001$, the interface evolves from its initially flat state into an unstable one as the fluctuating amplitude grows over time. Figures 3(j,k,l) demonstrate the reduction in the fluctuating amplitude as Kn increases, indicating a weakening of the interfacial instability.

At $Kn = 0.011$, the instability is no longer observable, and a reversal of the concentration field occurs at $t = 10\tau$. Our results suggest that the instability at the interface weakens with increasing Kn, and is totally suppressed beyond a critical value. Additionally, the interface thickness also increases with Kn, as is evident from figures 3(*d–f*), reflecting enhanced diffusion between light and heavy molecules at large Kn. This behaviour is consistent with the findings of Sagert *et al.* (2015).

https://doi.org/10.1017/jfm.2026.12225 Published online by Cambridge University Press

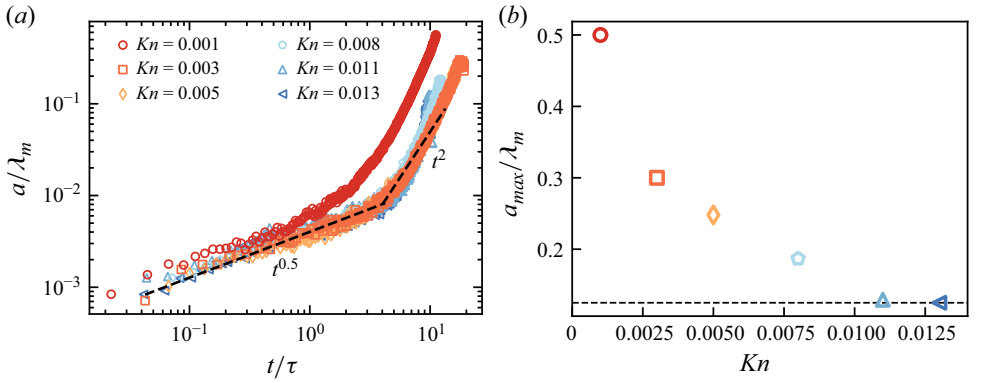


Figure 4. (*a*) Evolution of the perturbation amplitude a as a function of time for various Kn. The dashed lines represent the diffusive-growth scaling law $a \sim t^{0.5}$, and the self-similar growth scaling law $a \sim t^2$. (*b*) Maximum perturbation amplitude a_{max} at different Kn.

To quantitatively assess the influence of rarefaction on the instability, the fluctuating amplitude a as a function of time for various Kn is shown in figure 4. The fluctuating amplitude a is computed as the peak-to-trough distance of the low-pass filtered $\alpha_v = 0.5$ contour (Harrington 1993), where the filter window is $\lambda_m/20$, and λ_m is the most unstable wavelength. Figure 4(*a*) demonstrates that the growth rate of the fluctuating amplitude decreases as Kn increases. In the near-continuum regime, the growth of the fluctuating amplitude transitions from an initial diffusive regime, where $a/\lambda_m \sim t^{1/2}$, to a subsequent mixing regime with $a/\lambda_m \sim t^2$ (Taylor 1950; Wei & Livescu 2012; Gallis *et al.* 2016; Zhou *et al.* 2021).

For $Kn \gtrsim 0.011$, however, the initial amplitude growth is followed by decay, and the scaling of the mixing regime is absent. As shown in figures 3(*i*,*l*), this decay results from the interaction of the perturbation with the upper and lower domain boundaries. The maximum achieved amplitude a_{max}, plotted against Kn in figure 4(*b*), decreases with increasing Kn, and plateaus for $Kn \gtrsim 0.011$. This demonstrates that a larger Knudsen number suppresses perturbation growth, establishing $Kn \approx 0.011$ as the critical value for the onset of the RTI in this system.

3.2. *Mean squared displacement of molecules at different Kn*

To further elucidate how rarefied gases suppress interfacial instability in the RT system, we examine the molecular translational motion using the mean squared displacement (MSD), a standard measure of particle or object motion in dynamical systems (Michalet 2010; Huang *et al.* 2011; Peter 2011; Schirripa & Luin 2024). The molecular MSD is defined as

$$\langle \boldsymbol{r}^2(t) \rangle = \frac{1}{N} \sum_{i=1}^{N} [\boldsymbol{x}_i(t + \Delta t) - \boldsymbol{x}_i(t)]^2 , \tag{3.1}$$

where N is the number of particles, Δt is the lag time, and $\boldsymbol{x}_i(t)$ denotes the position of particle i at time t. Since gravitational acceleration and wall confinement strongly affect motion in the y-direction, the MSD is evaluated using only the x-direction displacement, which is periodic. This isolates molecular motion from gravitational and boundary influences, providing a clear characterisation of rarefaction-induced transport.

Figures 5(*a*,*b*) show the molecular trajectories over the same characteristic time $t = \tau$ for $Kn = 0.001$ and $Kn = 0.013$, respectively. The red and cyan dots denote the final

https://doi.org/10.1017/jfm.2026.12225 Published online by Cambridge University Press

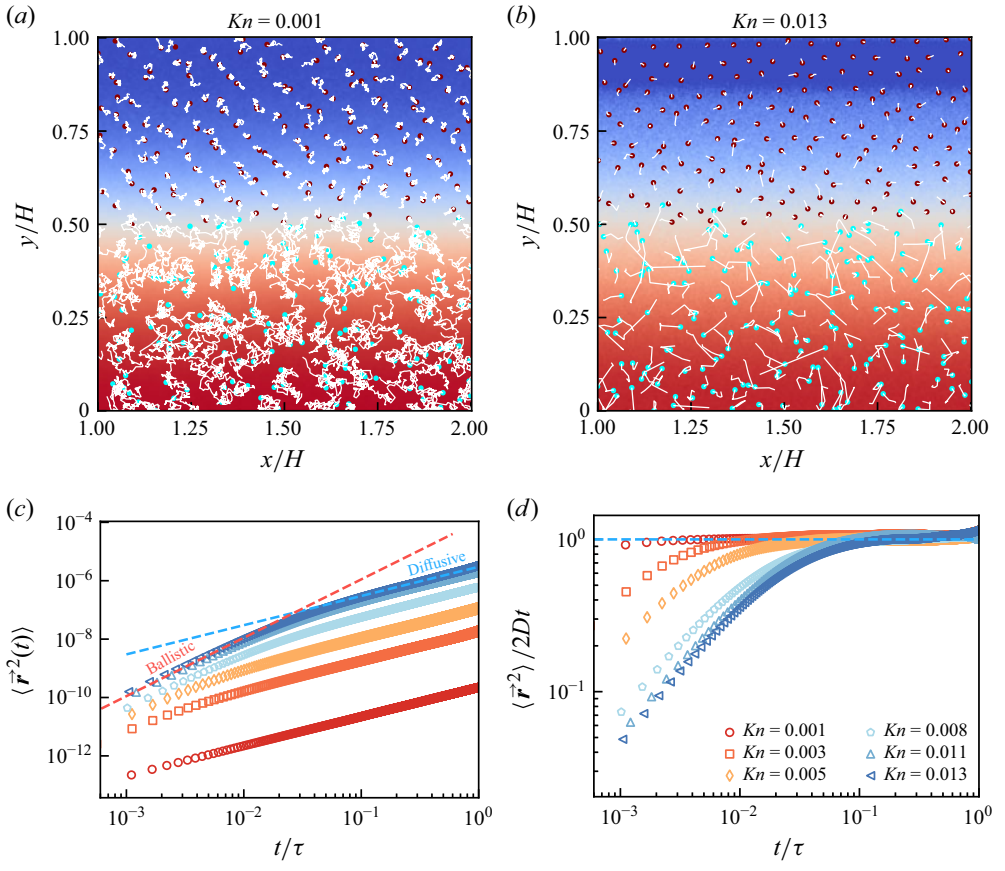


Figure 5. Trajectories of molecules: (*a*) $Kn = 0.001$ and (*b*) $Kn = 0.013$. The red and cyan dots represent the ending points of the trajectories of heavy and light fluid molecules, respectively. The background is the α_v field at $t = \tau$. (*c*) The MSD of molecules with time t/τ at different Kn. The blue and orange dashed lines indicate the diffusive scaling $\langle \boldsymbol{r}^2 \rangle \sim t$ and ballistic scaling $\langle \boldsymbol{r}^2 \rangle \sim t^2$, respectively. (*d*) Normalised MSD of molecules with time t/τ at different Kn.

positions of heavy and light fluid molecules, superimposed on the α_v field at $t = \tau$. Because the thermal velocity of the heavy molecules is lower than that of the light molecules, their displacement over the same time interval is correspondingly smaller. At $Kn = 0.001$, molecular trajectories display frequent directional changes, characteristic of collision-dominated molecular motion. Conversely, at $Kn = 0.013$, the trajectories are predominantly straight, indicating a transition towards ballistic transport over the same time scale.

This qualitative contrast is quantified in figure 5(*c*), which compares the MSD across different Knudsen numbers. At early times, the MSD follows the ballistic scaling, after which it gradually transitions to diffusive behaviour once a sufficient number of collisions have occurred. The diffusion coefficient D can be obtained via the classical Einstein relation for diffusion (Einstein 1905):

$$\langle \boldsymbol{r}^2(t) \rangle = 2Dt. \tag{3.2}$$

The MSD at different Kn is normalised by the corresponding diffusion coefficient, as shown in figure 5(*d*). As Kn increases, the characteristic time required for molecules to transition from ballistic to diffusive motion becomes longer. This behaviour indicates

https://doi.org/10.1017/jfm.2026.12225 Published online by Cambridge University Press

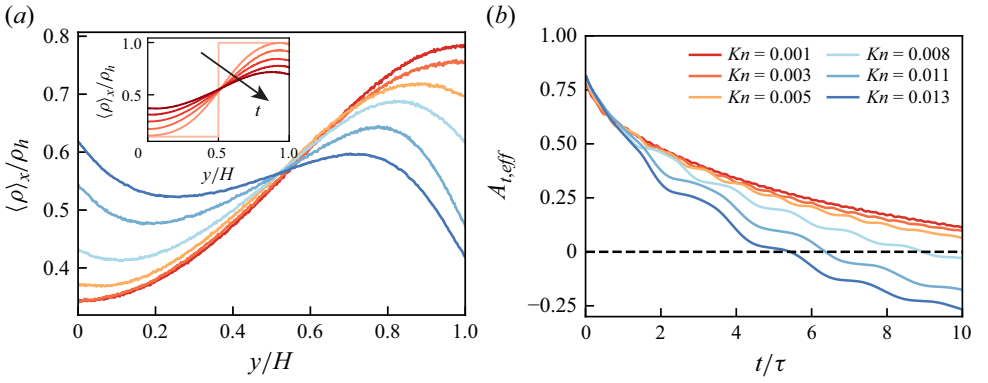


Figure 6. (*a*) Dimensionless density distribution with different Kn at $t = 5\tau$, where $\langle\rho\rangle_x$ is the average result in the x-direction. The inset shows the dimensionless density distribution with different times at $Kn = 0.005$. (*b*) Temporal evolution of the effective Atwood number $A_{t,eff}$ at different Kn.

that intermolecular collisions occur less frequently at large Kn, resulting in an extended duration of super-diffusive motion ($\langle \boldsymbol{r}^2(t)\rangle \sim t^{\zeta},\ \zeta > 1$).

3.3. *Flow field characteristics at different Kn*

How do molecular level alterations in rarefied gases influence macroscopic flow field characteristics? The density distribution from the flow field provides a direct measure of these molecular level effects. Figure 6(*a*) shows the flow field density distribution at $t = 5\tau$ for different Kn. Here, $\langle\rho\rangle_x$ denotes the density averaged in the x-direction, and ρ_h is the heavy fluid density at $t = 0$. The inset presents the temporal evolution of the dimensionless density at $Kn = 0.005$.

At the same characteristic time, the interfacial density gradient decreases as Kn increases, indicating that large Kn enhances diffusion within the RT system. This observation is consistent with the results shown in figure 3. Combined with the MSD results in figure 5, increasing the Kn promotes the super-diffusive behaviour of molecules, thereby enhancing interfacial mixing between light and heavy molecules. Macroscopically, this results in faster diffusion and a more rapid decay of the density gradient.

The effect of density distribution on instability can be quantified by the effective Atwood number $A_{t,eff}$. According to (2.6), A_t also determines the growth rate of interface perturbations. The effective Atwood number is defined as

$$A_{t,eff} = \frac{\langle\rho\rangle_t - \langle\rho\rangle_b}{\langle\rho\rangle_t + \langle\rho\rangle_b}, \tag{3.3}$$

where $\langle\rho\rangle_t$ and $\langle\rho\rangle_b$ denote the spatially averaged densities in $y > 0.5H$ and $y < 0.5H$, respectively. The temporal evolution of $A_{t,eff}$ for different Kn is shown in figure 6(*b*). The value of $A_{t,eff}$ gradually decreases over time, and this decay becomes steeper as Kn increases. For $Kn \geqslant 0.008$, $A_{t,eff}$ can even become negative. When $A_{t,eff} \leqslant 0$, the density distribution is completely reversed relative to the initial state, as confirmed by figure 3(*l*). From (2.6), it is evident that when $A_{t,eff} < 0$, the growth rate of the perturbation becomes imaginary. As demonstrated in § 3.2, the molecular MSD reveals that rarefaction significantly enhances the super-diffusive transport of molecules. Specifically, at higher Kn, the reduced collision frequency extends the duration of the ballistic regime, allowing molecules to travel longer distances without scattering. This enhanced molecular mobility facilitates rapid interfacial mixing between the heavy and light fluids. Consequently, this

https://doi.org/10.1017/jfm.2026.12225 Published online by Cambridge University Press

vigorous mixing at the molecular scale macroscopically manifests as an accelerated decay of the density gradient. The system transitions from a buoyancy-dominated regime to a diffusion-dominated regime so rapidly that the initial density stratification is destroyed before the RTI can develop, leading to the observed inversion of the concentration field.

Viscosity also plays an important role in the RT system. At a fixed reference temperature, the kinematic viscosity is inversely proportional to the density. Therefore, when the Knudsen number increases (due to the decrease in pressure), the density decreases, resulting in an increase in kinematic viscosity. This further suppresses the growth of interfacial instability perturbations for large Knudsen numbers. However, the condition whether A_t vanishes is not a sufficient criterion for stability, as instability may have already developed prior to the decay of the Atwood number. The key is the relative timing of instability onset and diffusive decay, a competition governed by the Knudsen number.

3.4. *Stability analysis*

In continuum RTI, interface growth transitions from an initial diffusive regime to a mixing regime (Wei & Livescu 2012; Gallis *et al.* 2016; Zhou 2017*a*; Gopalakrishnan *et al.* 2018). These regimes correspond physically to mass transport by diffusion and by buoyancy-driven convection. Consequently, mass transport in RTI evolves from diffusion-dominated to instability-dominated dynamics. However, at large Knudsen numbers, intermolecular diffusion is enhanced (Sagert *et al.* 2015; Keenan & Sauppe 2023; Guo *et al.* 2024), raising the question of whether instability can emerge against strong diffusive damping. To resolve this, we characterise the competition between diffusion and instability by defining two time scales: a diffusion time scale τ_D, and an instability time scale τ_I.

Through dimensional analysis of the diffusion equation, the diffusion width satisfies $a^2(t) \sim 2Dt$, where D is the diffusion coefficient. Since the present study considers diffusion primarily in the vertical direction, the corresponding diffusion time scale can be expressed as $\tau_D \approx a^2(t)/(2D_{12})$. Here, $a(t)$ is the instantaneous perturbation amplitude of the interface. This quantity is directly extracted from the DSMC results as the peak to trough vertical distance of the low-pass filtered $\alpha_v = 0.5$ concentration contour, as described in § 3.1. During the diffusive growth regime, the diffusion width $\sqrt{2D_{12}t}$ and the perturbation amplitude $a(t)$ remain of the same order of magnitude. The diffusion time scale τ_D characterises the time required for molecular diffusion to produce an interface displacement comparable to the instantaneous perturbation amplitude.

The instability time scale τ_I can be characterised by the growth rate γ (Youngs 1984). Taking into account the effect of viscosity and diffusion, the growth rate can be expressed as (Duff *et al.* 1962)

$$\gamma = \sqrt{\frac{A_t g k}{\psi} + \bar{\nu}^2 k^4} - (\bar{\nu} + D_{12})k^2, \tag{3.4}$$

where ψ is the growth suppression factor, with $\psi = 1$ at $t = 0$. Here, ψ represents the influence of the interface density gradient on stability, and it is obtained by solving the inviscid Rayleigh equation (Rayleigh 1883):

$$\frac{\mathrm{d}}{\mathrm{d}y}\left(\rho \frac{\mathrm{d}w}{\mathrm{d}y}\right) = wk^2\left(\rho - \frac{g}{\gamma_0^2}\frac{\mathrm{d}\rho}{\mathrm{d}y}\right), \quad \gamma^2 = \frac{A_t g k}{\psi}, \tag{3.5}$$

https://doi.org/10.1017/jfm.2026.12225 Published online by Cambridge University Press

where w is the perturbation velocity. The density ρ and its gradient $\mathrm{d}\rho/\mathrm{d}y$ are obtained using a self-similar model of density diffusion:

$$\rho(y,t)=\frac{1}{2}(\rho_h+\rho_l)\left[1+2A_t\sqrt{\pi}\int_0^{y/\epsilon}\exp\left(-\xi^2\right)\mathrm{d}\xi\right], \tag{3.6}$$

where the integral represents the error function with respect to y/ϵ, and the self-similar variable $\epsilon=\sqrt{4Dt}$ denotes the diffusion width at time scale t. Equation (3.6) is substituted into (3.5), and ψ is obtained numerically, following the procedure given in Duff *et al.* (1962). Therefore, the growth rate γ is obtained, and the instability time scale is defined as $\tau_I=1/\gamma$.

To calculate the growth suppression factor ψ at different Kn, the density distribution of the RT system varies differently over time at different Kn, therefore the self-similarity model for density distribution cannot be applied. The density and density gradient in (3.5) are obtained from the numerical results of DSMC simulations. The growth suppression factor ψ is computed through numerical iteration applied to (3.5) (Duff *et al.* 1962).

Figure 7(*a*) shows the growth-suppression factor ψ as a function of the dimensionless diffusion thickness $k\epsilon$ for different Kn, where the theoretical values are obtained using the self-similar density diffusion model in (3.6). For comparison, the corresponding continuum DNS results are obtained by solving the NS equations under the same initial and boundary conditions. The growth inhibition factor ψ obtained from DSMC and DNS agrees well with the theoretical prediction during the early stage of instability evolution in the near continuum regime. From a molecular perspective, ψ physically represents the efficiency of momentum transfer across the interface. In the near continuum regime (low Kn), frequent intermolecular collisions maintain a sharp density gradient, resulting in a lower ψ, and allowing hydrodynamic instabilities to develop. However, as rarefaction increases, the enhanced molecular mean free paths (as shown in the MSD analysis in § 3.2) promote direct molecular transport across the interface. This microscopic mixing diffuses the density gradient, effectively increasing ψ and damping instability growth. To calculate the growth rate γ at different Kn, the kinematic viscosity $\bar{\nu}$ and diffusion coefficient D_{12} in the rarefied gas are considered, which can be obtained from (2.4) and (2.5). The growth rate γ for different Kn was obtained by substituting the calculated ψ into (3.4).

Figure 7(*b*) shows the growth rate γ at different Kn. The growth rate decreases over time, and the larger the Kn value, the more rapidly the growth rate decays to zero. At late times, the growth rate becomes negative, indicating a decay of the perturbation amplitude. This behaviour is attributed to enhanced interfacial mixing under rarefied conditions, which weakens the density gradient and reduces the effective Atwood number, eventually causing diffusive transport to dominate instability growth. This implies that large Kn suppresses the growth of perturbations, which yields the same conclusion as that obtained in figure 6(*b*). Notably, the growth rate γ decreases as Kn increases at $t=0$. This is because a large Kn corresponds to a large most unstable wavelength, which has a small wavenumber and thus exhibits a small growth rate.

To determine whether instability overcomes diffusive damping, we examine the dimensionless time scale ratio $\beta\equiv\tau_D/\tau_I$, where τ_D is the diffusive time scale and τ_I is the instability time scale. When $\beta<1$, the diffusion time scale is shorter than the instability time scale, indicating that mass transport is dominated by diffusion at the interface. Conversely, $\beta>1$ indicates that the instability dominates. The temporal evolution of β at different Kn is shown in figure 7(*c*). For $Kn<0.011$, the value of β increases from less than 1 to greater than 1 over time, indicating that mass transport is dominated by a transition from diffusion to instability at the interface. For $Kn\gtrsim 0.011$, β

https://doi.org/10.1017/jfm.2026.12225 Published online by Cambridge University Press

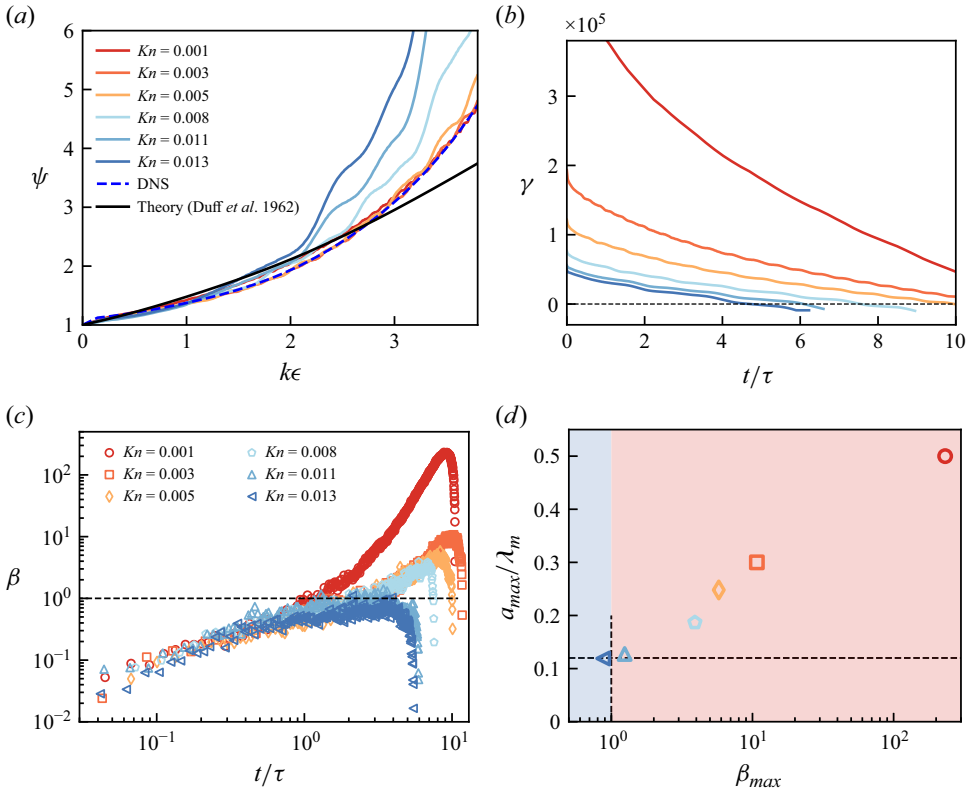


Figure 7. (*a*) Growth-suppression factor ψ as a function of $k\epsilon$ for different Kn. (*b*) The growth rate γ with time t at different Kn. (*c*) The ratio $\beta = \tau_D/\tau_I$ of the time scale of diffusion to the time scale of instability with time t at different Kn. (*d*) The maximum value a_{max}/λ_m of the dimensionless interface fluctuating amplitude versus β_{max} for different Kn.

remains below 1 throughout the evolution of the interface, indicating that mass transport is dominated by diffusion and does not transition to instability. This indicates that the critical Knudsen number for instability suppression in the present RT system is approximately $Kn_{cr} = 0.011$.

Figure 7(*d*) shows the dimensionless maximum value of the interface fluctuating amplitude (a_{max}/λ_m) as a function of the maximum time scale ratio β_{max}. Here, a_{max}/λ_m starts increasing when β_{max} becomes larger than 1. This again demonstrates that the proposed competition governs the emergence of instability.

3.5. *Influence of Froude number on RTI*

The previous subsections (§§ 3.1–3.4) examined the effect of the Knudsen number on the evolution of RTI at a fixed geometric ratio $H/\lambda_m = 0.5$, showing that rarefaction suppresses the instability, with a critical threshold at $Kn \approx 0.011$. In practical applications, however, the domain height H significantly affects the strength of the driving force, with its effect often represented by Fr. We therefore extend the analysis to investigate the combined effects of Fr and Kn on the stability of the rarefied RT system.

Figure 8 presents the instability regime diagram in the (Kn, Fr) parameter space. The parameter space is partitioned into three distinct regimes: (i) no instability development, (ii) rarefaction-induced suppression, and (iii) unstable growth. When $H/\lambda_m \lesssim 0.4$, the RTI

https://doi.org/10.1017/jfm.2026.12225 Published online by Cambridge University Press

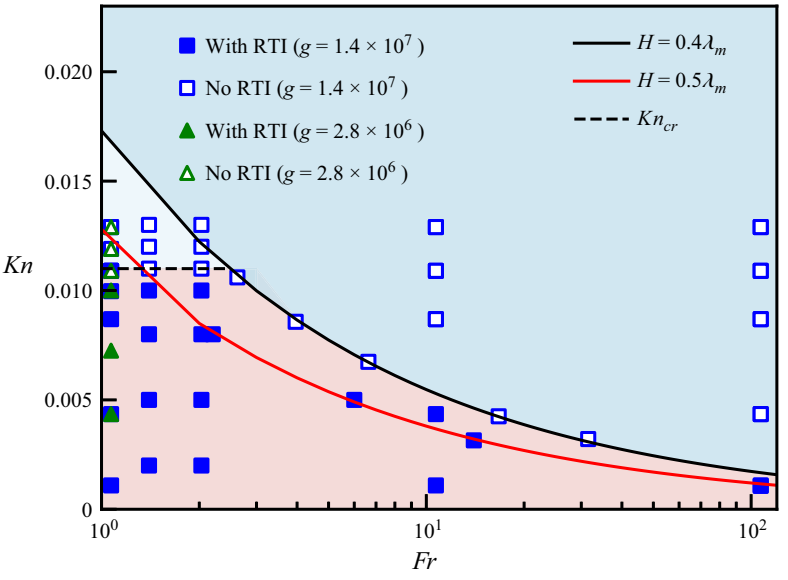


Figure 8. Instability regime diagram in the (Kn, Fr) parameter space for the rarefied RT system. The pink region denotes conditions where instability grows, while the blue region indicates suppression by rarefaction effects. The blue region represents cases where the domain height is insufficient to allow perturbations to evolve into the nonlinear stage before interacting with the boundaries. Solid squares indicate simulations where instability is observed, whereas hollow squares denote cases where no instability is detected. The green triangles highlight supplementary cases (cases 42–48) where the domain height H was increased and gravitational acceleration g was reduced proportionally to maintain a constant Fr, thereby verifying that the observed threshold is independent of absolute length scales.

fails to develop beyond the linear stage in the continuum regime (Wei & Livescu 2012). In this regime, the constrained domain size prevents perturbations from transitioning to the nonlinear growth. For $H/\lambda_m \gtrsim 0.4$, perturbations can evolve into the nonlinear regime, and instability suppression is governed predominantly by the Knudsen number. As established in § 3.4, when $Kn \gtrsim 0.011$, the instability is completely suppressed, irrespective of the domain size or Froude number. This behaviour aligns with the time scale competition framework, wherein molecular diffusion remains faster than instability growth throughout the evolution ($\beta = \tau_D/\tau_I < 1$).

To verify that this threshold is not an artefact of the specific domain configuration, additional simulations (cases 42–48) were performed and compared with cases 21–27 at fixed Fr. In these supplementary cases, indicated by the green triangles in figure 8, the gravitational acceleration was reduced by a factor of 5, while the domain height was increased proportionally. This approach maintained a constant Fr while varying the absolute length scales. The results confirm that the instability remains completely suppressed for $Kn \gtrsim 0.011$, consistent with the primary simulation set. This demonstrates that within the parameter range considered, the critical Knudsen number for instability suppression is independent of Fr, reinforcing that the stability threshold is determined by the competition between diffusive and instability time scales, rather than by geometric confinement effects.

4. Conclusions

In summary, we have systematically investigated the suppression of the Rayleigh–Taylor instability (RTI) in rarefied gases using GPU parallelised DSMC simulations across a

https://doi.org/10.1017/jfm.2026.12225 Published online by Cambridge University Press

broad range of Knudsen numbers. Our results establish $Kn \approx 0.011$ as a critical threshold; for $Kn \gtrsim 0.011$, interfacial instability is completely suppressed, and the maximum perturbation amplitude remains constant while the concentration profile undergoes rapid diffusion-driven reversal.

The consequence of rarefaction operates across scales. At the molecular level, increasing Kn extends the duration of super-diffusive motion, as is evident from the molecular mean squared displacement, delaying the transition to normal diffusion. At the macroscopic scale, this enhances interfacial mixing, rapidly weakening the density gradient and reducing the effective Atwood number that drives the instability.

Furthermore, the underlying physics of instability emergence is quantitatively captured by a time scale competition framework. We introduce a diffusion time scale τ_D and an instability time scale τ_I. Instability emerges only when $\tau_I < \tau_D$ (i.e. $\beta = \tau_D/\tau_I > 1$). For $Kn \gtrsim 0.011$, τ_D remains shorter than τ_I throughout the evolution ($\beta < 1$), confirming that diffusion perpetually dominates, and instability cannot develop – consistent with the observed saturation of the perturbation amplitude. Thus the transition to instability in rarefied RTI is governed by the competition between molecular diffusion and buoyant growth, leading to a critical Kn that dictates the stability of the system.

Finally, we have also identified two distinct regimes for RTI suppression: geometric confinement ($H/\lambda_m \lesssim 0.4$) prevents instability by restricting perturbation growth, while for larger domains ($H/\lambda_m \gtrsim 0.4$), suppression occurs when $Kn \gtrsim 0.011$ regardless of Fr. Validation across different gravitational accelerations confirms that the critical Knudsen number is independent of Fr, reinforcing that instability onset is governed by the competition between diffusive and instability time scales.

This study establishes a framework for predicting flow stability in rarefied gases by linking molecular transport to macroscopic instability thresholds. The proposed mechanism can be extended to other instabilities, such as Richtmyer–Meshkov, Kelvin–Helmholtz and shear-flow transitions, offering a general approach to probe the microscopic origins of hydrodynamic instability. A long-term challenge is to construct a unified theory connecting discrete molecular dynamics to continuum instability phenomena across microscopic, mesoscopic and macroscopic scales.

Funding. This work is supported by the NSFC Excellence Research Group Programme for 'Multiscale problems in nonlinear mechanics' (no. 12588201). It was also supported by the Natural Science Foundation of China under grant nos 12372219, 52450304, 12432011, 12422208, 12421002 and 12372220.

Declaration of interests. The authors report no conflict of interest.

References

Ahlers, G., Grossmann, S. & Lohse, D. 2009 Heat transfer and large scale dynamics in turbulent Rayleigh–Bénard convection. *Rev. Mod. Phys.* **81** (2), 503–537.

Bakshi, V. 2006 *EUV Sources for Lithography*. SPIE Press.

Betti, R., Goncharov, V.N., McCrory, R.L. & Verdon, C.P. 1998 Growth rates of the ablative Rayleigh–Taylor instability in inertial confinement fusion. *Phys. Plasmas* **5**, 1446–1454.

Betti, R. & Hurricane, O.A. 2016 Inertial-confinement fusion with lasers. *Nat. Phys.* **12**, 435–448.

Bird, G.A. 1963 Approach to translational equilibrium in a rigid sphere gas. *Phys. Fluids* **6**, 1518–1519.

Bird, G.A. 1989 Perception of numerical methods in rarefied gasdynamics. *Prog. Aerosp. Sci.* **117**, 211–226.

Bird, G.A. 1994 *Molecular Gas Dynamics and the Direct Simulation of Gas Flows*. Oxford University Press.

Boffetta, G. & Mazzino, A. 2017 Incompressible Rayleigh–Taylor turbulence. *Annu. Rev. Fluid Mech.* **49**, 119–143.

Bouras, I., El, A., Fochler, O., Niemi, H., Xu, Z. & Greiner, C. 2012 Transition from ideal to viscous Mach cones in a kinetic transport approach. *Phys. Lett. B* **710** (4), 641–646.

Cercignani, C. 1988 *The Boltzmann Equation and its Applications*. Springer.

https://doi.org/10.1017/jfm.2026.12225 Published online by Cambridge University Press

CHILLÀ, F. & SCHUMACHER, J. 2012 New perspectives in turbulent Rayleigh–Bénard convection. *Eur. Phys. J. E* **35** (7), 58.

CHONG, K.-L., WANG, B.-F., WANG, F., YAN, R., DING, H., SUN, C. & ZHOU, Q. 2026 Flow physics and modeling in extreme ultraviolet sources. *Natl Sci. Rev.* **13**, nwag298.

COOK, A.W., CABOT, W. & MILLER, P.L. 2004 The mixing transition in Rayleigh–Taylor instability. *J. Fluid Mech.* **511**, 333–362.

DUFF, R.E., HARLOW, F.H. & HIRT, C.W. 1962 Effects of diffusion on interface instability between gases. *Phys. Fluids* **5** (4), 417–425.

EINSTEIN, A. 1905 Über die von der molekularkinetischen Theorie der Wärme geforderte Bewegung von in ruhenden Flüssigkeiten suspendierten Teilchen. *Ann. Phys.* **322** (8), 549–560.

FEI, F., ZHANG, J., LI, J. & LIU, Z.-H. 2020 A unified stochastic particle Bhatnagar–Gross–Krook method for multiscale gas flows. *J. Comput. Phys.* **400**, 108972.

GAD-EL-HAK, M. 1999 The fluid mechanics of microdevices – the Freeman Scholar Lecture. *Trans. ASME J. Fluids Engng* **121**, 5–33.

GALLIS, M.A., KOEHLER, T.P., TORCZYNSKI, J.R. & PLIMPTON, S.J. 2016 Direct simulation Monte Carlo investigation of the Rayleigh–Taylor instability. *Phys. Rev. Fluids* **1** (4), 043403.

GALLIS, M.A., TORCZYNSKI, J.R., KRYGIER, M.C., BITTER, N.P. & PLIMPTON, S.J. 2021 Turbulence at the edge of continuum. *Phys. Rev. Fluids* **6**, 013401.

GALLIS, M.A., TORCZYNSKI, J.R., RADER, D.J., TIJ, M. & SANTOS, A. 2006 Normal solutions of the Boltzmann equation for highly nonequilibrium Fourier flow and Couette flow. *Phys. Fluids* **18** (1), 017104.

GARCIA, A.L. 1986 Nonequilibrium fluctuations studied by a rarefied-gas simulation. *Phys. Rev. A* **34** (2), 1454–1457.

GLADKOV, D., TAPIA, J.J., ALBERTS, S. & D'SOUZA, R.M. 2012 Graphics processing unit based direct simulation Monte Carlo. *Simulation* **88** (6), 680–693.

GONCHAROV, V.N. 2002 Analytical model of nonlinear, single-mode, classical Rayleigh–Taylor instability at arbitrary Atwood numbers. *Phys. Rev. Lett.* **88** (13), 134502.

GOPALAKRISHNAN, S.S., CARBALLIDO-LANDEIRA, J., KNAEPEN, B. & DE WIT, A. 2018 Control of Rayleigh–Taylor instability onset time and convective velocity by differential diffusion effects. *Phys. Rev. E* **98** (1), 011101.

GORJI, M.H., TORRILHON, M. & JENNY, P. 2011 Fokker–Planck model for computational studies of monatomic rarefied gas flows. *J. Fluid Mech.* **680**, 574–601.

GOSHAYESHI, B., DI STASO, G., TOSCHI, F. & CLERCX, H.J.H. 2020 Numerical study of heat transfer in Rayleigh–Bénard convection under rarefied gas conditions. *Phys. Rev. E* **102** (1), 013102.

GUO, Y., WU, D. & ZHANG, J. 2024 Effects of mass diffusion on Rayleigh–Taylor instability under a large gravity. *Phys. Plasmas* **31** (11), 112106.

HARRINGTON, R.F. 1993 *Field Computation by Moment Methods*. Wiley–IEEE Press.

HUANG, R.-X., CHAVEZ, I., TAUTE, K.M., LUKIĆ, B., JENEY, S., RAIZEN, M.G. & FLORIN, E.L. 2011 Direct observation of the full transition from ballistic to diffusive Brownian motion in a liquid. *Nat. Phys.* **7** (7), 576–580.

ISOBE, H., MIYAGOSHI, T., SHIBATA, K. & YOKOYAMA, T. 2015 Filamentary structure on the Sun from the magnetic Rayleigh–Taylor instability. *Nature* **434**, 478–481.

JANKA, H.T. 2012 Explosion mechanisms of core-collapse supernovae. *Annu. Rev. Nucl. Part. Sci.* **62**, 407–451.

KADAU, K., BARBER, J.L., GERMANN, T.C. & ALDER, B.J. 2008 Scaling of atomistic fluid dynamics simulations. *Phys. Rev. E* **78** (4), 045301.

KADAU, K., BARBER, J.L., GERMANN, T.C., HOLIAN, B.L. & ALDER, B.J. 2010 Atomistic methods in fluid simulation. *Phil. Trans. R. Soc. Lond. A* **368**, 1547–1560.

KADAU, K., GERMANN, T.C., HADJICONSTANTINOU, N.G., LOMDAHL, P.S., DIMONTE, G., HOLIAN, B.L. & ALDER, B.J. 2004 Nanohydrodynamics simulations: an atomistic view of the Rayleigh–Taylor instability. *Proc. Natl Acad. Sci. USA* **101** (16), 5851–5855.

KADAU, K., ROSENBLATT, C., BARBER, J.L., GERMANN, T.C., HUANG, Z.B., CARLÈS, P. & ALDER, B.J. 2007 The importance of fluctuations in fluid mixing. *Proc. Natl Acad. Sci. USA* **104** (19), 7741–7745.

KASHKOVSKY, A.V., KUDRYAVTSEV, A.N. & SHERSHNEV, A.A. 2019 Numerical simulation of the Rayleigh–Taylor instability in rarefied Ar/He mixture using the direct simulation Monte Carlo method. *J. Phys.: Conf. Ser.* **1382** (1), 012154.

KEENAN, B.D. & SAUPPE, J.P. 2023 Improved analytic modeling of the linear Rayleigh–Taylor instability with plasma transport. *Phys. Plasmas* **30** (7), 072106.

KOURA, K. & MATSUMOTO, H. 1992 Variable soft sphere molecular model for air species. *Phys. Fluids* **4** (5), 1083–1085.

https://doi.org/10.1017/jfm.2026.12225 Published online by Cambridge University Press

LARROCHE, O., RINDERKNECHT, H.G., ROSENBERG, M.J., HOFFMAN, N.M., ATZENI, S., PETRASSO, R.D., AMENDT, P.A. & SÉGUIN, F.H. 2016 Ion-kinetic simulations of D-3He gas-filled inertial confinement fusion target implosions with moderate to large Knudsen number. *Phys. Plasmas* **23** (1), 012701.

LAYZER, D. 1955 On the instability of superposed fluids in a gravitational field. *Astrophys. J.* **122**, 1.

LI, Z.-H., PENG, A.-P., WU, J.-L., MA, Q., TANG, X.-W. & LIANG, J. 2019 Gas-kinetic unified algorithm for computable modeling of Boltzmann equation for aerothermodynamics during falling disintegration of Tiangong-type spacecraft. *AIP Conf. Proc.* **2132** (1), 100013.

LIAO, S.-J. & QIN, S.-J. 2022 Large-scale influence of numerical noises as artificial stochastic disturbances on a sustained turbulence. *J. Fluid Mech.* **948**, A7.

LIAO, S.-J. & QIN, S.-J. 2025 Noise-expansion cascade: an origin of randomness of turbulence. *J. Fluid Mech.* **1009**, A2.

LIVESCU, S., ROY, R.V. & SCHWARTZ, L.W. 2011 Leveling of thixotropic liquids. *J. Non-Newtonian Fluid Mech.* **166** (7), 395–403.

LOHSE, D. & SHISHKINA, O. 2023 Ultimate turbulent thermal convection. *Phys. Today* **76** (11), 26–32.

LOHSE, D. & SHISHKINA, O. 2024 Ultimate Rayleigh–Bénard turbulence. *Rev. Mod. Phys.* **96** (3), 035001.

LOHSE, D. & XIA, K.-Q. 2010 Small scale properties of turbulent Rayleigh–Bénard convection. *Annu. Rev. Fluid Mech.* **42**, 335–364.

MA, Q., YANG, C.-X., CHEN, S., FENG, K.-K., CUI, Z.-Q. & ZHANG, J. 2024 Effect of thermal fluctuations on spectra and predictability in compressible decaying isotropic turbulence. *J. Fluid Mech.* **987**, A29.

MA, X., DELAMERE, P.A. & OTTO, A. 2015 Plasma transport driven by the Rayleigh–Taylor instability. *J. Geophys. Res.: Space Phys.* **121** (6), 5260–5271.

MCGUIRE, W.J. 1996 Volcano instability: a review of contemporary themes. *Geol. Soc. Spec. Publ.* **110** (1), 1–23.

MCMULLEN, R.M., KRYGIER, M.C., TORCZYNSKI, J.R. & GALLIS, M.A. 2022 Navier–Stokes equations do not describe the smallest scales of turbulence in gases. *Phys. Rev. Lett.* **128** (11), 114501.

MCMULLEN, R.M., KRYGIER, M.C., TORCZYNSKI, J.R. & GALLIS, M.A. 2023 Molecular-gas-dynamics simulations of turbulent Couette flow over a mean-free-path-scale permeable substrate. *Phys. Rev. Fluids* **8**, 083401.

MICHALET, X. 2010 Mean square displacement analysis of single-particle trajectories with localization error: Brownian motion in an isotropic medium. *Phys. Rev. E* **82** (4), 041914.

MIKAELIAN, K.O. 2014 Solution to Rayleigh–Taylor instabilities: bubbles, spikes, and their scalings. *Phys. Rev. E* **89** (5), 053009.

NORMAN, P., VALENTINI, P. & SCHWARTZENTRUBER, T. 2013 GPU-accelerated classical trajectory calculation direct simulation Monte Carlo applied to shock waves. *J. Comput. Phys.* **247**, 153–167.

PETER, N.P. 2011 Brownian motion goes ballistic. *Science* **332** (6031), 802–803.

RAO, S.J. & BASU, S. 2026 Secondary atomization of droplets at extreme conditions. *Annu. Rev. Fluid Mech.* **58**, 83–110.

RAYLEIGH, LORD 1883 Investigation of the character of the equilibrium of an incompressible heavy fluid of variable density. *Proc. Lond. Math. Soc.* **s1-14** (1), 170–177.

RISTORCELLI, J.R. & CLARK, T.T. 2004 Rayleigh–Taylor turbulence: self-similar analysis and direct numerical simulations. *J. Fluid Mech.* **507**, 213–253.

SAGERT, I., BAUER, W., COLBRY, D., HOWELL, J., STABER, A. & STROTHER, T. 2014 Kinetic simulations of Rayleigh–Taylor instabilities. *J. Phys.: Conf. Ser.* **535** (1), 012032.

SAGERT, I., HOWELL, J., STABER, A., STROTHER, T., COLBRY, D. & BAUER, W. 2015 Knudsen-number dependence of two-dimensional single-mode Rayleigh–Taylor fluid instabilities. *Phys. Rev. E* **92** (1), 013009.

SCHIRRIPA, S.C. & LUIN, S. 2024 Trajectory analysis in single-particle tracking: from mean squared displacement to machine learning approaches. *Intl J. Mol. Sci.* **25** (16), 8660.

SHARP, D.H. 1984 An overview of Rayleigh–Taylor instability. *Physica D* **12** (1), 3–18.

SHERSHNEV, A.A., KUDRYAVTSEV, A.N. & KASHKOVSKY, A.V. 2023 Numerical simulation of the Rayleigh–Taylor instability in rarefied mixture of monatomic gases using continuum and kinetic approaches. *AIP Conf. Proc.* **2504** (1), 030111.

SHERSHNEV, A.A., KUDRYAVTSEV, A.N., KASHKOVSKY, A.V., BORISOV, S.P. & POLESHKIN, S.O. 2024 Numerical simulation of rarefied flow instabilities using kinetic approach. *Supercomput. Front. Innov.* **11** (2), 65–77.

SHISHKINA, O. 2021 Rayleigh–Bénard convection: the container shape matters. *Phys. Rev. Fluids* **6** (9), 090502.

https://doi.org/10.1017/jfm.2026.12225 Published online by Cambridge University Press

STEFANOV, S.K., BARBER, R.W. & OTA, M. 2005 Comparison between Navier–Stokes and DSMC calculations for low Reynolds number slip flow past a confined microsphere. *AIP Conf. Proc.* **762** (1), 701–706.

STEVENS, A.B. & HRENYA, C.M. 2005 Comparison of soft-sphere models to measurements of collision properties during normal impacts. *Powder Technol.* **154** (2), 99–109.

SU, W., ZHU, L.-H., WANG, P., ZHANG, Y.-H. & WU, L. 2020 Can we find steady-state solutions to multiscale rarefied gas flows within dozens of iterations? *J. Comput. Phys.* **407**, 109245.

TAYLOR, G.I. 1950 The instability of liquid surfaces when accelerated in a direction perpendicular to their planes. *Proc. R. Soc. Lond. A* **201** (1065), 192–196.

THEOFANOUS, T.G., LI, G.J. & DINH, T.N. 2004 Aerobreakup in rarefied supersonic gas flows. *J. Fluids Engng* **126** (4), 516–527.

WEI, T. & LIVESCU, D. 2012 Late-time quadratic growth in single-mode Rayleigh–Taylor instability. *Phys. Rev. E* **86** (4), 046405.

WUNSCH, C. & FERRARI, R. 2004 Vertical mixing, energy, and the general circulation of the oceans. *Annu. Rev. Fluid Mech.* **36**, 281–314.

XIA, K.-Q., CHONG, K.-L., DING, G.-Y. & ZHANG, L. 2025 Some fundamental issues in buoyancy-driven flows with implications for geophysical and astrophysical systems. *Acta. Mechanica Sin.* **41** (1), 324287.

XIA, K.-Q., HUANG, S.-D., XIE, Y.-C. & ZHANG, L. 2023 Tuning heat transport via coherent structure manipulation: recent advances in thermal turbulence. *Natl Sci. Rev.* **10** (6), nwad012.

XU, K. & HUANG, J.-C. 2010 A unified gas-kinetic scheme for continuum and rarefied flows. *J. Comput. Phys.* **229** (20), 7747–7764.

YOUNGS, D.L. 1984 Numerical simulation of turbulent mixing by Rayleigh–Taylor instability. *Physica D* **12** (1), 32–44.

ZHANG, M.-L., GUO, Z.-F., LIU, J.-Q., LIU, G.-M., ZHANG, L.-H., LEI, M., ZHAO, W.-B., MA, L., SEPE, V. & VENTURA, G. 2018 The intraplate Changbaishan volcanic field (China/North Korea): a review on eruptive history, magma genesis, geodynamic significance, recent dynamics and potential hazards. *Earth-Sci. Rev.* **187**, 19–52.

ZHOU, Q., HUANG, Y.-X., LU, Z.-M., LIU, Y.-L. & NI, R. 2016 Scale-to-scale energy and enstrophy transport in two-dimensional Rayleigh–Taylor turbulence. *J. Fluid Mech.* **786**, 294–308.

ZHOU, Q. & JIANG, L.-F. 2016 Kinetic and thermal energy dissipation rates in two-dimensional Rayleigh–Taylor turbulence. *Phys. Fluids* **28** (4), 045109.

ZHOU, Y. 2017*a* Rayleigh–Taylor and Richtmyer–Meshkov instability induced flow, turbulence, and mixing. I. *Phys. Rep.* **720**, 1–136.

ZHOU, Y. 2017*b* Rayleigh–Taylor and Richtmyer–Meshkov instability induced flow, turbulence, and mixing. II. *Phys. Rep.* **723**, 1–160.

ZHOU, Y., *et al.* 2021 Rayleigh–Taylor and Richtmyer–Meshkov instabilities: a journey through scales. *Physica D* **423**, 132838.

https://doi.org/10.1017/jfm.2026.12225 Published online by Cambridge University Press